Formation, Time–Temperature–Transformation curves and magnetic properties of FeCoNbSiBP metallic glasses

Formation, Time-Temperature-Transformation curves and Magnetic Properties of FeCoNbSiBP metallic glasses

G. Fiore [1,#], M. Baricco [1], L. Martino [2], M. Coisson [2], P. Tiberto [2], F. Vinai [2], L. Battezzati[1]

[1] Dipartimento di Chimica e Centro Superfici ed Interfacce Nanostrutturate (NIS), Università di Torino, Via Pietro Giuria 7,10125 Torino, Italy

[2] Istituto Nazionale di Ricerca Metrologica (INRIM), Divisione Elettromagnetismo, Strada delle Cacce 91, 10135 Torino, Italy

[#]Corresponding author: gianluca.fiore@unito.it

Keywords: X-ray diffraction, DSC, metallic glasses, Fe base alloys, rapid solidification, magnetic properties

Abstract

Starting from the $Fe_{52}Co_{23}Nb_4Si_5B_{16}$ alloy having good soft magnetic properties and tendency to amorphization, the addition of P, a glass former in Fe-based alloys, is explored up to 4% at.

The alloys were rapidly solidified by means of planar flow casting and have been characterized using scanning electron microscopy (SEM), X-ray diffraction (XRD), differential scanning calorimetry (DSC) and high temperature differential thermal analysis (HT DSC). The crystallization mechanism has been studied as a function of temperature: it involves primary formation of a bcc phase at low P content and becomes eutectic at 4% P. A remarkable achievement are Time-Temperature-Transformation (TTT) diagrams for primary crystallization obtained by DSC. Magnetisation measurements as a function of temperature in parallel with thermal analysis revealed

details of the crystallization sequence. The magnetic softness of alloys has been shown with hysteresis cycles.

The use of P appears favourable to amorphization, thermal and magnetic properties up to 2 at%.

1. Introduction

Magnetic alloys play a central role in technological innovation because of their use as electro-magnetic materials in various devices and appliances. Property optimization justifies such an enduring interest in the light of the need of high efficiency devices, e. g. transformers, in which soft magnetic alloys play a key role in both power generation and conversion. As a consequence, reduction of power losses is still extremely important.

Fe based glassy alloys (BGAs) are useful in a wide range of applications because they exhibit many unique properties, including high strength, large elastic strain limit, high hardness, good soft magnetic behavior, viscous flow workability in the supercooled liquid region, homogeneity on the nanometer scale and corrosion resistance [1,2,3]. In this context, (Fe, Co)-based alloys have been intensively investigated as bulk soft magnetic materials for high-temperature applications [4,5] since controlled addition of Co enhances the Curie temperature. Moreover, good magnetic properties are found at high temperature due to the presence of (Fe, Co, Si) nanograins [6]. Here, by bulk we intend materials having minimum size in excess of some tens of microns to be contrasted by thin films of nanometre size.

New metallic glasses based on the (Fe, Co)-B-Si-Nb system have been reported where Nb is used to improve the glass forming ability (GFA) of the alloy. These glasses also display excellent mechanical strength combined with magnetic properties [7-15]. Minor addition of alloy components appears then an effective tool to get better GFA [16].

The aim of this work is to evaluate the effect of adding P to the above system and to increase the Fe content in partial substitution of Co with respect to previous works, on alloy constitution,

microstructure, thermal behaviour, and magnetic properties. The use of P is justified by the fact that it is a known glass former in Fe-based alloys in combination with B, apparently inducing similar short range order and atomic cluster connectivity [17,18] and proved useful in improving the thermal stability of (Fe, Co)-Mo-B-Si metallic glasses [19]; we note also that its bonding energy with all metallic constituents is strongly negative [20,21].

2. Materials and Methods

Master alloys with nominal composition (atomic percent) $Fe_{52}Co_{23}Nb_4Si_5B_{16}$ (named MA), $Fe_{52}Co_{23}Nb_4Si_5B_{15}P_1$ (named 1P), $Fe_{52}Co_{23}Nb_4Si_5B_{14}P_2$ (named 2P) and $Fe_{51}Co_{22}Nb_4Si_5B_{14}P_4$ (named 4P) were prepared by arc-melting pre-alloyed Fe-B-Si and Fe-P with pure Co, Nb and Si elements in Ar atmosphere with Ti and Zr getters.

Ribbon samples 1 cm wide and some tens of micrometers thick were obtained in a planar flow casting apparatus under Ar atmosphere, the velocity of the wheel was 25 m/s.

Microstructure analysis has been carried out using a Leica Stereoscan 420 Scanning Electron Microscope (SEM) and phase composition was checked by Energy Dispersive X-ray Spectroscopy (EDS). XRD patterns were collected using Co Kα and Cu Kα radiation to examine the structure of the master alloys, of the as-quenched and annealed ribbons.

Melting and solidification of alloys have been monitored by using a Setaram HT-DSC at the scanning rate of 0.166 Ks^{-1}. Phase transformations of the ribbons were studied by Differential Scanning Calorimetry (DSC) up to 973 K; all DSC runs were performed under flowing Ar at the scanning rates of 0.05 Ks^{-1} and 0.333 Ks^{-1}.

Magnetisation properties as a function of temperature and applied magnetic field (80 kA/m) have been determined by means of a Vibrating Sample Magnetometer (VSM, LakeShore 7410) in the temperature interval from 300 K to 1200 K and field from - 10 kOe to 10 kOe at the scanning rate

of 0.033 Ks^{-1}. Hysteresis loops were measured by a digital feedback wattmeter under sinusoidal induction waveform [22] at the frequency of 500 Hz.

3. Results and Discussion

3.1 Alloy phase constitution and melting-solidification behaviour

The phase constitution of the alloys has been determined at all processing steps to identify both equilibrium and metastable phases which might compete with glass formation. The diffraction patterns of all master alloys (Fig. 1) display textured reflections due to α-Fe(Co,Si) with lattice parameter of 2.847 Å, $(Fe,Co)_2B$ with lattice parameters a = 5.099 Å and c = 4.235 Å and a third phase not identified so far; possibly a (Co,Fe)Nb(P,B) compound. In fact, as the amount of P increase, the reflections of the latter phase shift to lower values of the scattering vector suggesting that it exists in a range of composition. This multinary phospho-boride is apparently promoted by Nb which has strong negative value of enthalpy of mixing with P (-81 kJ/mol [20,21]). Since the reflections of $(Fe,Co)_2B$ remain at the same angle when P partially substitutes for B in the alloy, it is deduced that P preferentially segregates into the Nb-containing phase. The phases identified in master alloys represent apparently the equilibrium alloy constitution since they were found also in ribbons annealed at the end of all transformation steps (see below).

The solidification microstructure of all the alloys consists of primary dendrites of α-Fe(Co,Si), facetted crystals of the compounds and a eutectic made of the α-Fe(Co,Si) and the Nb-rich compound (Fig. A).

HTDSC melting curves are shown in Fig. 2 and the relevant thermal properties are collected in Table 1. The thermal profile of all alloys presents the same behaviour with a major endothermic

peak due to eutectic melting and a broad signal ending at the liquidus. The liquidus temperature has a minimum for the composition with 1 % at. P and then increases showing that the P addition causes departure from the eutectic composition (Tab. 1). The exothermic signal seen before the onset of melting of the 4P alloy (Fig. 2b) indicates the transformation of a metastable phase, still retained after the synthesis up to high temperature.

After melt quenching, diffraction patterns taken both on the wheel and air side (not reported here) show the ribbons are amorphous within the limit of detection of the technique.

3.2 Devitrification process and phase evolution

The DSC traces given by portions of the ribbons are shown in Fig. 3 (a-d) and thermophysical data are given in Table 1. All ribbons exhibit a glass transition followed by crystallization that takes place in either one or two stages as a function of composition. The first peak starts soon after the onset of the glass transition in all cases. With the increase in P content, the second exothermic peak gradually shifts to lower temperatures. The traces for MA, 1P and 2P are similar, whereas a change in crystallization mode is suggested by the shape of the peak of 4P (Fig. 3 d). From Tab. 1 and Fig. 3 it is deduced that the Curie temperature, T_c, and glass transition temperature, T_g, shift to lower values as the amount of P increases. The decrease in T_c for the 4P alloy is more apparent because it contains 1 % less Fe and 1 % less Co. The crystallization temperature, T_x, similarly decreases with the exception of the 4P ribbon whose T_x value is the highest (Fig. 3 d). The thermal parameters usually employed to rank the GFA of alloys, the extent of the supercooled liquid region ($\Delta T_x = T_x - T_g$) and the reduced glass transition temperature (T_g/T_l), have opposite trend as a function of P content: the former increases while the latter decreases. It cannot be concluded then that the addition of P causes substantial change in GFA. The DSC traces of 2P and 4P alloys display a further exothermal effect after completion of crystallization indicating again the occurrence of

metastable crystalline products. The total heat evolved during the two stages of transformation, ΔH_x, (Tab. 1) is comparable for all alloys within the experimental uncertainty.

Fig. 4 shows the diffraction patterns of the ribbons heated up to the end of the first calorimetric crystallization peak. Up to 2 at. % P, the crystallization process consists in the partial devitrification of the amorphous matrix with formation of a primary phase, α-Fe type (Fig. 4 a-c) with lattice parameter a = 2.857 Å. Further P addition ($Fe_{51}Co_{22}Nb_4Si_5B_{14}P_4$ alloy) results in a eutectic devitrification producing simultaneously α-Fe type and H phases (Fig. 4 d). The H phase has hexagonal structure and has been reported as rhombohedral distorsion of the α-Mn type cubic structure [23]. It has already been found during the early stages of crystallization of Fe-Si-B-Nb alloys with more than ~8 at.% B and low content of Nb (0.5 ÷ 4 at.%) [24].

These results differ from previous literature reports on alloys based on the Fe-Co-Nb-Si-B system having Fe:Co ratio of 50:50 [13,14] and 30:70 [12]. The first crystallization step of these alloys richer in Co involves the formation of the metastable complex-cubic phase $Fe_{23}B_6$. This highlights further the possible occurrence of various crystal phases in this multinary system and their role in phase selection with respect to the amorphous one.

Diffraction patterns of the MA, 1P and 2P ribbons heated up to the second crystallization peak (Fig. B) show that it involves the full devitrification of the residual amorphous matrices, with formation of the H phase (Fig. B a-c). The intensity of the reflections of the α-Fe type phase decreases with increasing P content while those of the H phase become predominant showing a change in the relative amount of the two phases. The exothermic peaks displayed in the DSC traces of 2P and 4P at the highest temperatures are due to the formation of the $Fe_{23}B_6$ type compound and an unindexed phase (Fig. C).

The XRD reflections of the α-Fe phase shift to high Q values during the progression of crystallization indicating that the primary α phase is initially Fe rich and then incorporates Co when the H and $Fe_{23}B_6$ phase are formed (Fig. 4 a-c, d).

Table 2 summarizes the phases obtained at different crystallization steps of the initially amorphous ribbons.

Magnetization versus temperature curves were obtained in order to follow the occurrence of magnetic phases during the amorphous-to-crystalline transformation. The temperature dependence of the magnetic moment M is shown in Fig. 5 for all compositions. The Curie temperature of the amorphous phases occur at about 670 K for the 0P, 1P and 2P ribbons while it is found at about 630 K for the 4P alloy. Such values are in good agreement with those obtained by DSC (Fig. 3). When the temperature is further increased, the magnetisation remains close to zero in a temperature interval where the amorphous matrix is paramagnetic and does not incur in any structural transformation. Above approximately 800 K, M starts increasing, indicating that magnetic precipitates are forming within the amorphous matrix. These precipitates are identified with the α-Fe type phase of high Curie temperature mentioned above whose volume fraction an amount of Co increase as a consequence of the progress of transformations, giving rise to an increase of magnetisation. The magnetic behaviour confirms that the crystallisation process occurs in two steps, as clearly indicated by the two broad peaks in each of the M vs. T curves in Fig. 5 apart from the 4P sample for which a single peak is found. It is noteworthy that the two peaks mark stages of precipitation of new magnetic crystals and possibly coarsening of existing ones. Even if the development of hard magnetic phases is expected above approximately 900 K, as evidenced by XRD and DSC data, they cannot be detected with the measured M vs. T curves, as their Curie temperature is lower than this [25-29].

3.3 Isothermal crystallization and TTT curves

The first crystallization process was studied in isothermal condition by annealing portions of ribbons at 803 K , i. e. close to the glass transition range and more than 30 degrees below the crystallization onset, for different times with the aim of studying the nanocrystallization of the α-Fe

phase inside the amorphous matrix and the possible related improvement of soft magnetic properties. Such analysis was performed only on MA and 1P ribbons. The other two compositions were excluded because of the diverse character of crystallization of 4P, and of the superposition of the two crystallization steps in 2P which does not allow the control of the primary transformation in suitable time and temperature ranges.

The size of scattering domains of the bcc phase has been determined from diffraction patterns of samples annealed for different times (Fig. 6 a and b). The halo due to the amorphous matrix and the (110) reflection of the α solid solution have been fitted by means of a Gaussian and a pseudo-Voigt function, respectively. The Rietveld refinement method has been employed to get the domain size.

At 803 K, the domains grow to 16 nm in 6 minutes and 21 nm in about 18 minutes reaching a steady size of 23 nm after 20 min (Fig. 7).

The annealed ribbons then were scanned in DSC at 20 K/min in order to check for their thermal behaviour (Figs. 8 a and b). As the primary devitrification progresses, the amorphous matrix changes composition with a consequent shift of the Curie temperature to higher values (arrows in Figs. 8 a and b). This is consistent with the early precipitation of an α phase relatively rich in Fe (Fig. 4), that leaves the amorphous matrix enriched in Co which increases the Curie temperature.

Comparing the DSC traces of samples annealed for various amounts of time, it is noted that after two hours, both alloys have reached the end of the first crystallization step since no significant changes appear in DSC traces anymore. Such results are confirmed by the residual heats of crystallization (inset of Fig. 8a) and the Curie temperatures which do not appreciably change for annealing times longer than two hours.

Isothermal DSC measurements were employed to get a TTT curve for primary crystallization. To reach this goal the samples were at first annealed up to temperatures in the range 783-803 K to obtain full relaxation of the glass. Attention has been paid in avoiding the formation of crystals during this annealing stage. The isothermal crystallization temperatures were reached at 300 K/min checking carefully that the temperature of the samples did not overshoot. With these precautions,

well defined exothermic calorimetric signals were obtained in the above range of temperatures. Examples of calorimetric traces of two subsequent isothermal runs are reported in the inset of Fig. 9. The first one relates to the amorphous sample held isothermally up to complete crystallization. The second one, performed after the first one, provides a baseline to the exothermal peak. Such result is rare for primary crystallization which often starts during the heating up stage of the calorimeter. This has been attributed to the predominance of growth of quenched-in nuclei over further nucleation [30]. Apparently in the present cases nucleation is predominant with a rather long incubation time at temperature close to Tg.

In Fig. 9 the times required for reaching the onset of the crystallization (open circle and close squares for MA and 1P respectively) at each isothermal temperature are reported giving a TTT plot for the start of transformation. They are rather short if compared with those of a good glass formers [31] but enough to allow a proper control of the process. Note that the 1% P addition has no effect on the resistance against crystallization since the onsets of the transformations are the same within the experimental uncertainty.

3.4 Magnetic properties

Hysteresis loops of the annealed MA and 1P ribbons are reported in Fig. 10 (a and b). For comparison, hysteresis loops of as spun and relaxed ribbons (at 523 K for 1 hour) are also given. They are characterised by a slower approach to saturation magnetization that is typical of an amorphous structure. As soon as crystals nuclei are formed, magnetization suddenly reaches saturation with an average value of 1 T. In the inset, an enlargement of the magnetisation curves is reported in order to put in evidence the evolution of the coercivity field (H_c) as a function of thermal treatments. The H_c behaviour as a function of annealing time at $T_a = 803$ K for compositions having 0% P and 1% P is then reported in Fig.11. Here, H_c is seen to be almost the same for both compositions in the as-prepared condition and to increase with increasing annealing time. However,

the presence of P induces slightly higher H_c values in the composition containing 1% P with respect to the one with no Phosphorous. Such a result is generally justified by the coarsening of crystalline precipitates hindering the domain wall motion. However, this hypothesis is not confirmed by microstructural data in the present case. As a consequence, such an increment must be accounted for by the remaining amorphous phase having higher magnetic anisotropy value.

In addition, in Figs. 10 and 11 it is noted that the H_c values of both ribbons remain low (about 5 Am^{-1}) when the scattering domain size is below 16 nm. As indicated by DSC and M vs. T measurements, before totally transforming the amorphous in crystalline phase the increase in P content favours the Co enrichment of the bcc phase inducing a slight increase of the coercive field while maintaining high values of magnetisation saturation.

The additional crystalline phases formed after completing the transformation to the fully crystalline state should be magnetically hard, as confirmed by the hysteresis loops (not reported here) measured at room temperature after completion of crystallization, with coercive field values of the order of 10^3 A/m, typical of samples containing Fe-B or Fe-P phases [32].

4. Conclusions

The effect of adding Phosphorus to the quinary $Fe_{52}Co_{23}Nb_4Si_5B_{16}$ on phase constitution, glass formation and magnetic properties has been studied in alloys od the following composition: $Fe_{52}Co_{23}Nb_4Si_5B_{15}P_1$, $Fe_{52}Co_{23}Nb_4Si_5B_{14}P_2$, and $Fe_{51}Co_{22}Nb_4Si_5B_{14}P_4$. Differences are slight although significant. The paper gives account of the results of all processing steps from the production of master alloys, to rapid solidification and annealing.

The microstructure of the all master alloys is constituted by three phases. Two of these, identified as α-Fe(Co,Si) phase and $(Fe,Co)_2B$, are common to all alloys. The third one is a ternary FeNbB compound in the quinary alloy, whereas, it has been identified as a (Fe,Co)Nb(B,P) phospho-boride in the case of the alloys containing P which must not be a stoichiometric compound since it has

been found to have variable composition as a function of P content. This feature might be detrimental for glass formation together with the increase in the liquidus temperature.

Fully amorphous ribbons were obtained by rapid solidification as confirmed by XRD and DSC. ΔT_x values increase as the amount of P increases, however, the GFA is not really improved since the value of the reduced glass transition temperature (T_g/T_l) decreases because of higher liquidus points. Up to 2 at. % P addition the crystallization process consists in the primary devitrification of the amorphous matrix with formation of α-Fe(Co, Si) phase suggesting the possibility of improving the soft magnetic properties via suitable precipitation anneals. Further P addition results in eutectic-like full devitrification of the glass. To this purpose, careful DSC work has provided TTT curves for primary crystallization of $Fe_{52}Co_{23}Nb_4Si_5B_{16}$ and $Fe_{52}Co_{23}Nb_4Si_5B_{15}P_1$ in a temperature range close to the glass transition region but below the onset of crystallization of a bcc α-Fe(Co, Si) solid solution.

The ribbons display saturation magnetization typical of amorphous and nanocrystalline structures. Annealed samples without P and with 1 at% P have comparable magnetic properties: the saturation magnetization reaches 1 T and coercivity fields are around 5 Am^{-1}. The use of higher P content is not only detrimental to the GFA but also induces crystallization of multiple phases, including a high melting compound, instead of primary α-Fe(Co, Si). The increase in P content favours the Co enrichment in the bcc phase. Magnetization versus temperature curves complemented DSC analyses unveiling details of the phase transformation up to the Curie temperature of the crystal phases rich in Co.

Acknowledgments

At UNITO this work is performed in the frame of the EU-7FP project ACCMET.

Fondazione S. Paolo is acknowledged for support to CdE NIS.

Referecences

[1] A. Inoue, N. Nishiyama, New Bulk Metallic Glasses for Applications as Magnetic-Sensing, Chemical, and Structural Materials, MRS Bull. 32 (2007) 651-658.

[2] N. Nishiyama, K. Amiya, A. Inoue, Bulk Metallic Glasses for Industrial Products, Mater. Trans. 45 (2004) 1245-1250.

[3] G. Herzer, Modern Soft Magnets: Amorphous and Nanocrystalline Materials, Acta Mater. 61 (2013) 718–734.

[4] M.E. McHenry, D.E. Laughlin, Nano-Scale Metarials Development for Future Magnetic Applications, Acta Mater. 48 (2000) 223-238.

[5] M.A. Willard, M.Q. Huang, D.E. Laughlin, M.E. McHenry, J.O. Cross, V.G. Harris, C. Franchetti, Magnetic Properties of HITPERM $(Fe,Co)_{88}Zr_7B_4Cu_1$ Magnets, J. Appl. Phys. 85 (1999) 4421-4423.

[6] C. Gomez-Polo, J.I. Perez-Landazabal, V. Recarte, J. Campo, P. Marın, M. Lopez, A. Hernando, M. Vazquez, High-temperature magnetic behavior of FeCo-based nanocrystalline alloys

Phys. Rev. B 66 (2002) 12401.

[7] A. Inoue, B. Shen, Formation and Soft Magnetic Properties of Co-Fe-Si-B-Nb Bulk Glassy Alloy, Mater. Trans. 43 (2002) 1230-1234.

[8] Y. Fu, B.L. Shen, H. Kimura, A. Makino, A. Inoue, Enhanced glass-forming ability of FeCoBSiNb bulk glassy alloys prepared using commercial raw materials through the optimization of Nb content, J. Appl. Phys. 107 (2010) 09A315

[9] A. Inoue, B.L. Shen, C.T. Chang, Super-high strength of over 4000 MPa for Fe-based bulk glassy alloys in $[(Fe_{1-x}Co_x)_{0.75}B_{0.2}Si_{0.05}]_{96}Nb_4$ system, Acta Mater. 52 (2004) 4093-4099.

[10] Q. Man, H. Sun, Y. Dong, B. Shen, H. Kimura, A. Makino, A. Inoue, Enhancement of glass-forming ability of CoFeBSiNb bulk glassy alloys with excellent soft-magnetic properties and superhigh Intermetallics 18 (2010) 1876–1879.

[11] H. Sun, Q. Man, Y. Dong, B. Shen, H. Kimura, A. Makino, A. Inoue, Effect of Nb addition on the glass-forming ability, mechanical and soft-magnetic properties in $(Co_{0.942}Fe_{0.058})_{72-x}Nb_xB_{22.4}Si_{5.6}$ bulk glassy alloys, J. Alloys Compd. 504S (2010) S31–S33.

[12] J. Fornell, S. González, E. Rossinyol, S. Suriñach, M.D, Baró, D.V. Louzguine-Luzgin, J.H. Perepezko, J. Sort, A. Inoue, Enhanced mechanical properties due to structural changes induced by devitrification in Fe–Co–B–Si–Nb bulk metallic glass, Acta Mater. 58 (2010) 6256-6266.

[13] M. Stoica, R. Li, A.R. Yavari, G. Vaughan, J. Eckert, N. Van Steenberge, D.R. Romera, Thermal stability and magnetic properties of FeCoBSiNb bulk metallic glasses, Journal of Alloys and Compounds 504S (2010), J. Alloys Compd. 504S (2010) S123-128.

[14] A. Inoue, B.L. Shen, C.T. Chang, Fe- and Co-based bulk glassy alloys with ultrahigh strength of over 4000MPa**,** Intermetallics 14 (2006) 936-944.

[15] T. Bitoh, A. Makino, A. Inoue, A.L. Greer, Large bulk soft magnetic $[(Fe_{0.5}Co_{0.5})_{0.75}B_{0.20}Si_{0.05}]_{96}Nb_4$ glassy alloy prepared by B_2O_3 flux melting and water quenching, Appl. Phys. Lett. 88 (2006) 182510.

[16] Wang WH, Roles of minor additions in formation and properties of bulk metallic glasses, Prog. Mater. Sci. 52 (2007) 540-596.

[17] M. Dekker, Rapidly solidified alloys, H.H. Liebrmann, New York, 1993.

[18] A. Inoue, A. Makino, T. Mizushima, Ferromagnetic bulk glassy alloys J. Magn. Magn. Mater. 215 (2000) 246-252.

[19] S. Bhattacharya, E. A. Lass, S. J. Poon, G. J. Shiflet, M. Rawlings, M. Daniil, M. A. Willard, Magnetic properties and thermal stability of (Fe,Co)-Mo-B-P-Si metallic glasses, J. Appl. Phys. 111 (2012) 063906

[20] A. Takeuchi, A. Inoue, Classification of Bulk Metallic Glasses by Atomic Size Difference, Heat of Mixing and Period of Constituent Elements and Its Application to Characterization of the Main Alloying ElementMater. Trans. 46 (2005) 2817-2829.

[21] F.R. de Boer, R. Boom, W.C.M. Matterns, A.R. Miedema, A.K. Niessen, Cohesion in Metals, North-Holland, Elsevier Science Publishers B.V, Amsterdam, 1988.

[22] G. Bertotti, E. Ferrara, F. Fiorillo, M. Pasquale, Loss measurements on amorphous alloys under sinusoidal and distorted induction waveform using a digital feedback technique, J. Appl. Phys. **73** (1993) 5375-5377.

[23] I.V. Lyasotsky, N.B. Dyakonova, E.N. Vlasova, D.L.Dyakonov, M. Yu. Yazvitskii, Metastable and quasiperiodic phases in rapidly quenched Fe-B-Si-Nb(Cu) alloys, Phys. Stat. Sol. (a) 203 (2006) 259-270.

[24] I.V. Lyasotsky, N.B. Dyakonova, D.L. Dyakonov, Metastable primary precipitation phases in multicomponent glass forming Fe-base alloys with metalloids, J. Alloys Comp. 586 (2014) S20-S23.

[25] C. Li, X. Tian, X. Chen, A.G. Ilinsky, K. Shi, Crystallization behavior of co-containing FINEMET amorphous alloy melt-spun ribbon, Mater. Lett. 60 (2006) 309-312.

[26] L.K. Varga, E. Bakos, L.F. Kiss, I. Bakonyi, The kinetics of amorphous-nanocrystalline transformation for a finemet alloy, Mater. Sci. Eng. A 179/180 (1994) 567-571.

[27] S. Linderoth, Annealing studies of ultrafine amorphous Fe-B alloy particles, J. Magn. Magn. Mater. 104-107 (1992) 128-130.

[28] M.E. McHendy, F. Johnson, H. Okumura, T. Ohkubo, V.R.V. Ramanan, D.E. Laughlin, the kinetics of nanocrystallization and microstructural observations in Finemet, Nanoperm and Hitperm nanocomposite magnetic materials, Scr. Mater. 48 (2003) 881-887.

[29] S.N. Kane, S. Tripathi, M. Coisson, E.S. Olivetti, P. Tiberto, F. Vinai, M. Baricco, G. Fiore, A. Apolinario, C.T. Sousa, J.P. Araujo, L.K. Varga, Microstructure and magnetic properties of $(Fe_{100-x}Co_x)_{84.5}Nb_5B_{8.5}P_2$ alloys, J. Alloys Comp. 536S (2012) S337-S341.

[30] J.H. Perepezko, J. Hamann, R.J. Hebert, H. Rösner, G. Wilde, Amorphization and devitrification reactions in metallic glass alloysMater. Sci. Eng. A 449–451 (2007) 84–89.

[31] G. Fiore, P. Rizzi, L. Battezzati, Phase constitution and glass formation in an Au-based alloy, J. Alloys Compd. 509 (2011) S166-S169

[32] F. Pfeifer, C. Radeloff, Soft magnetic Ni-Fe and Co-Fe alloys. Some physical and metallurgical aspects, J. Magn. Magn. Mater. 19 (1980) 190-207.

Captions:

Tab. 1 Thermal properties obtained from HTDSC and DSC. T_c: Curie temperature; T_m eutectic temperature; T_l liquidus temperature; ΔH_f enthalpy of fusion; $T_{g\ onset}$ glass transition temperature; T_x crystallization temperature; T_g/T_l reduced glass transition temperature; ΔH_x enthalpy of crystallization.

Tab. 2 Crystalline phase forming at the different stage of crystallization

Fig. 1 XRD patterns of: $Fe_{52}Co_{23}Nb_4Si_5B_{16}$ (a.), $Fe_{52}Co_{23}Nb_4Si_5B_{15}P_1$ (b.), $Fe_{52}Co_{23}Nb_4Si_5B_{14}P_2$ (c.) and $Fe_{51}Co_{22}Nb_4Si_5B_{14}P_4$ (d.) master alloys.

Fig. 2 High temperature DSC traces of Fe52Co23Nb4Si5B16 (a.), and Fe51Co22Nb4Si5B14P4 (b.) determined at the rate of 0.167 K/s.

Fig. 3 DSC traces of amorphous ribbons: $Fe_{52}Co_{23}Nb_4Si_5B_{16}$ (a.), $Fe_{52}Co_{23}Nb_4Si_5B_{15}P_1$ (b.), $Fe_{52}Co_{23}Nb_4Si_5B_{14}P_2$ (c.) and $Fe_{51}Co_{22}Nb_4Si_5B_{14}P_4$ (d.). Arrows indicate T_c. Dashed lines show the baseline used for peaks integrations.

Fig. 4 XRD patterns of the ribbons heated up to the end the first calorimetric crystallization peak: (a.) $Fe_{52}Co_{23}Nb_4Si_5B_{16}$, (b.) $Fe_{52}Co_{23}Nb_4Si_5B_{15}P_1$, (c.) $Fe_{52}Co_{23}Nb_4Si_5B_{14}P_2$ and (d.) $Fe_{51}Co_{22}Nb_4Si_5B_{14}P_4$.

Fig. 5 Magnetization relative to the room temperature value versus temperature of amorphous ribbons: (▼) $Fe_{52}Co_{23}Nb_4Si_5B_{16}$, (□) $Fe_{52}Co_{23}Nb_4Si_5B_{15}P_1$, (○) $Fe_{52}Co_{23}Nb_4Si_5B_{14}P_2$ and (▷) $Fe_{51}Co_{22}Nb_4Si_5B_{14}P_4$. Insert: Curve magnification showing the onset of crystallization.

Fig. 6 Diffraction patterns of the 0P ribbons (a) and 1P ribbons (b) annealed at 803 K for different times.

Fig. 7 The size of scattering domains of the primary α-Fe(Co,Si) phase crystallized in (○) $Fe_{52}Co_{23}Nb_4Si_5B_{16}$ (0P) and (■) $Fe_{52}Co_{23}Nb_4Si_5B_{15}P_1$ (1P) versus annealing time at 803 K.

Fig. 8 DSC traces (obtained at 20 $Kmin^{-1}$) of the 0P ribbons (a) and 1P ribbons (b) annealed at different times. Arrows indicate T_c. Insert of fig 4a: plot of the residual heat of crystallization as a function of the annealing time for 0P and 1P ribbons.

Fig. 9 TTT plot for the onset of the crystallization of (○) $Fe_{52}Co_{23}Nb_4Si_5B_{16}$ and (■) $Fe_{52}Co_{23}Nb_4Si_5B_{15}P_1$ ribbons. Insert: isothermal DSC traces of the amorphous sample (1° run) and the crystallized sample (2° run) used as reference.

Fig. 10 Hysteresis loops of the amorphous, relaxed and annealed $Fe_{52}Co_{23}Nb_4Si_5B_{16}$ (a) and $Fe_{52}Co_{23}Nb_4Si_5B_{15}P_1$ (b) ribbons.

Fig. 11 Coercive field as a function of annealing time at T_a=803 K for samples having (○) 0% and (■) 1% P content.

Fig. A Back-scattered SEM images of the master alloys cross-section: a. $Fe_{52}Co_{23}Nb_4Si_5B_{16}$ (named MA), b. $Fe_{52}Co_{23}Nb_4Si_5B_{15}P_1$ (named 1P), c. $Fe_{52}Co_{23}Nb_4Si_5B_{14}P_2$ (named 2P) and d. $Fe_{51}Co_{22}Nb_4Si_5B_{14}P_4$ (named 4P).

Fig. B XRD patterns of the ribbons heated up to the end the second calorimetric crystallization peak: (a.) $Fe_{52}Co_{23}Nb_4Si_5B_{16}$, (b.) $Fe_{52}Co_{23}Nb_4Si_5B_{15}P_1$, (c.) $Fe_{52}Co_{23}Nb_4Si_5B_{14}P_2$ and (d.) $Fe_{51}Co_{22}Nb_4Si_5B_{14}P_4$.

Fig. C XRD patterns of the ribbons heated up to 973 K: (a.) $Fe_{52}Co_{23}Nb_4Si_5B_{14}P_2$ and (b.) $Fe_{51}Co_{22}Nb_4Si_5B_{14}P_4$.

	Master alloys				Ribbons					
	T_c (K)	T_m (K)	T_l (K)	ΔH_f (J/g)	T_c (K)	$T_{g\ onset}$ (K)	T_x (K)	ΔT_x (K)	T_g/T_l	ΔH_x (J/g)
0P	1177	1349	1495	295 ± 7	676	810	840	30	0.542	80 ± 5
1P	1172	1344	1490	300 ± 7	670	791	838	42	0.531	85 ± 4
2P	1181	1356	1516	294 ± 7	665	783	830	47	0.516	87 ± 5
4P	1157	1326	1648	315 ± 10	631	804	851	53	0.488	79 ± 5

Tab. 1

Ribbon Sample	I crystallization step	II crystallization step	III crystallization step
0P	Amo + α-Fe '	α-Fe" + H	
1P	Amo + α-Fe '	α-Fe" + H	
2P	Amo + α-Fe '	α-Fe" + H	α-Fe"' + H + $Fe_{23}B_6$
4P	α-Fe '+ H		α-Fe" + H' + $Fe_{23}B_6$

Tab. 2

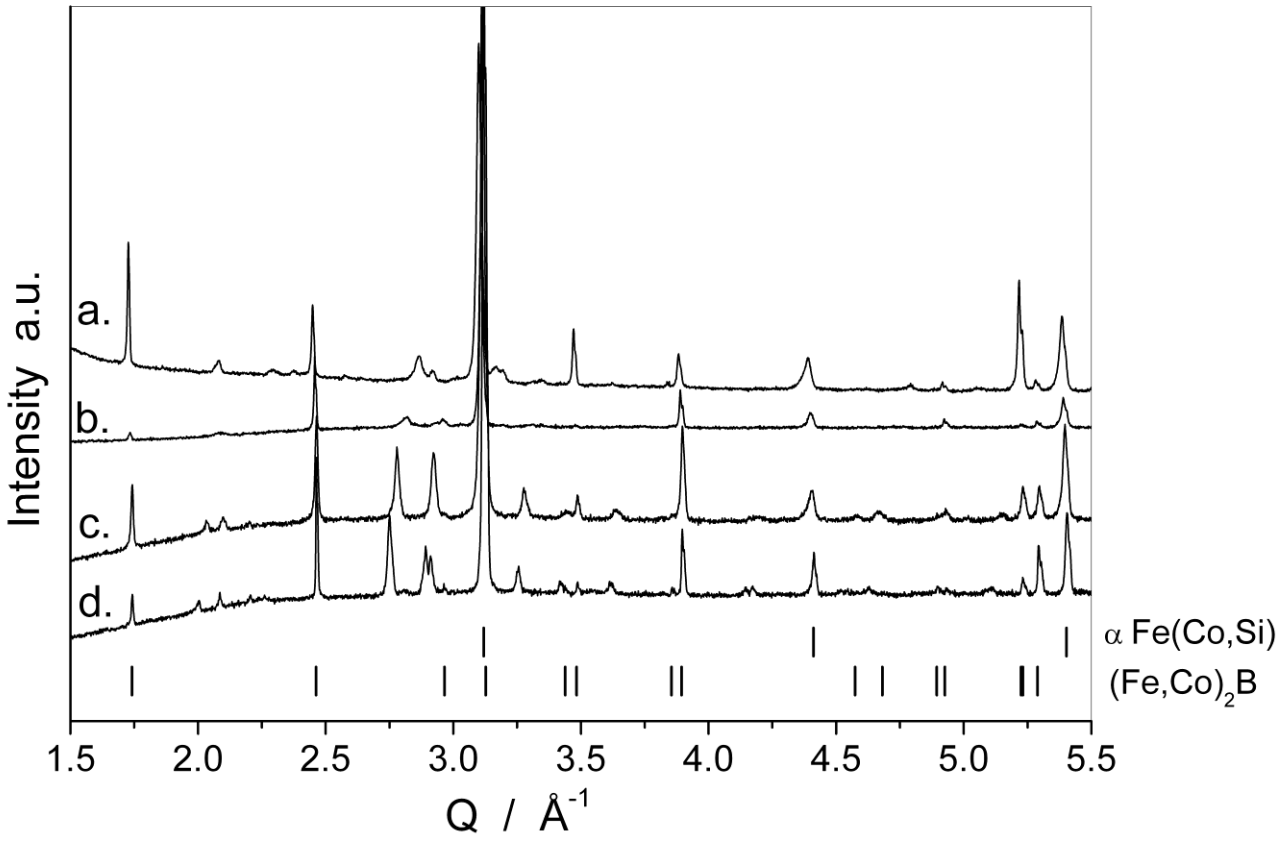

Fig. 1

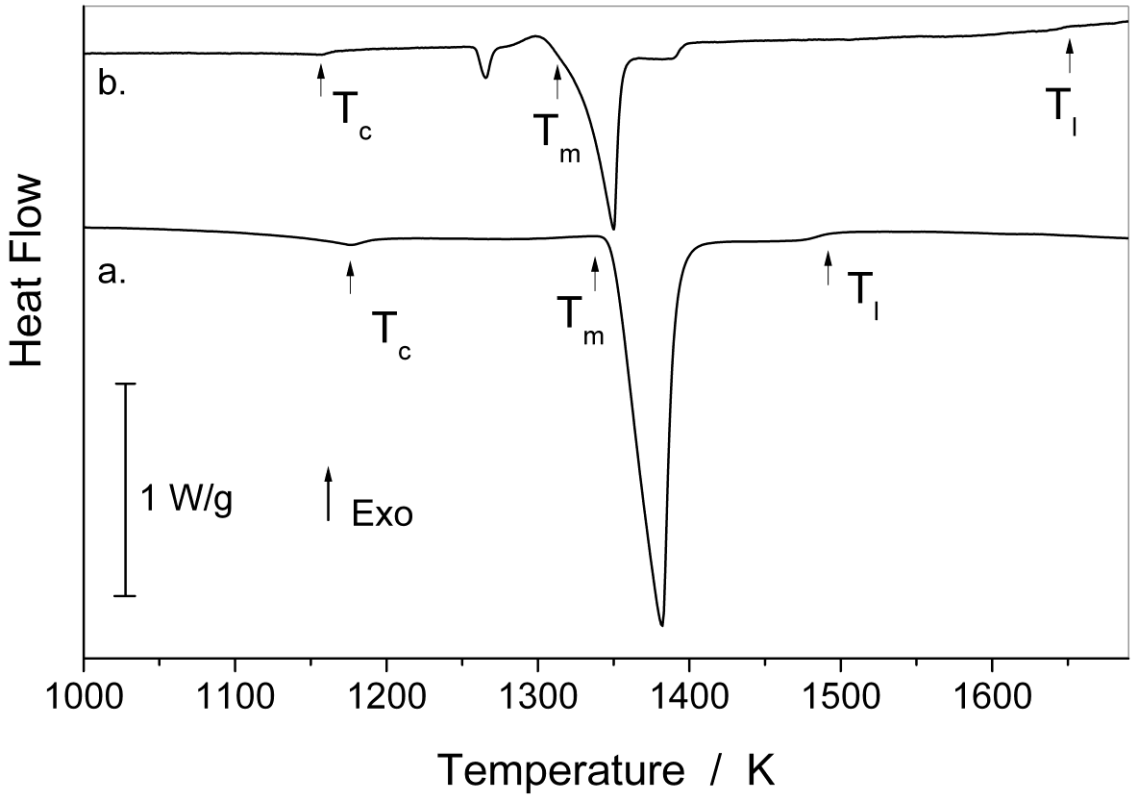
b.
a.
T_c
T_m
T_l
1 W/g
Exo
Heat Flow
1000
1100
1200
1300
1400
1500
1600
Temperature / K

Fig. 2

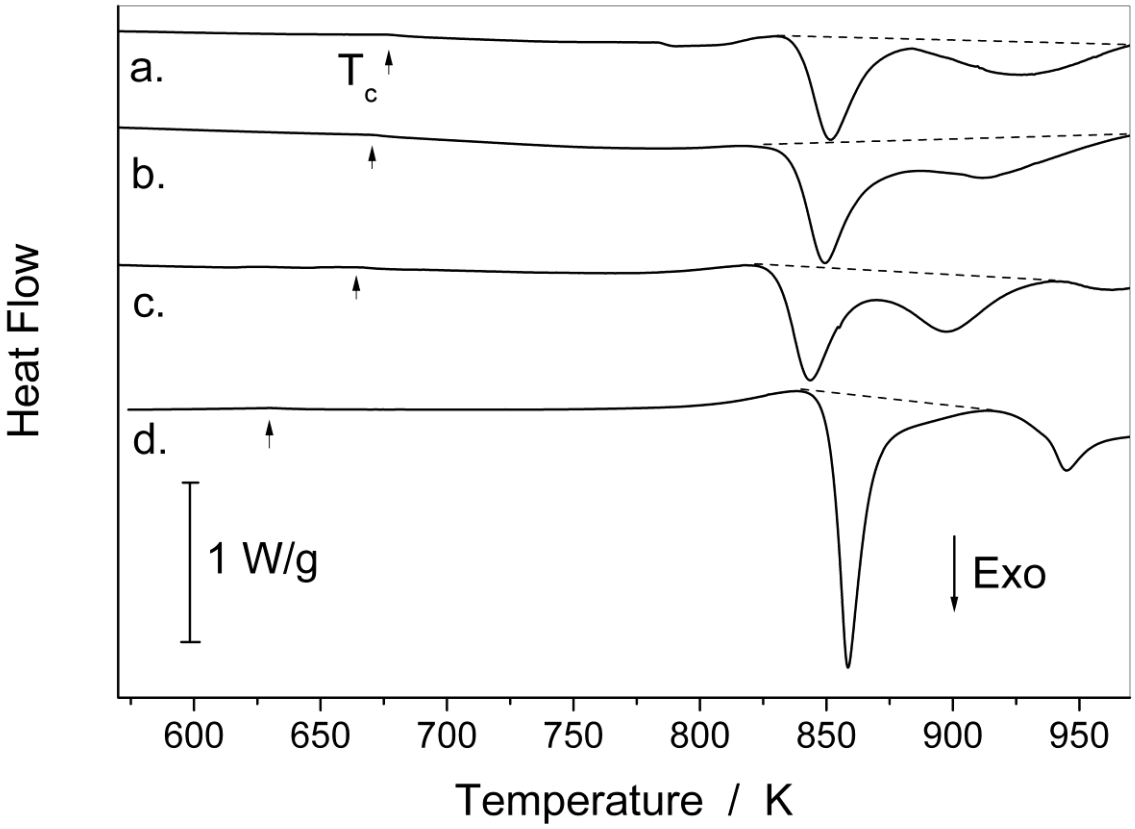
a.
T_c
b.
c.
d.
1 W/g
Exo
Heat Flow
600
650
700
750
800
850
900
950
Temperature / K

Fig. 3

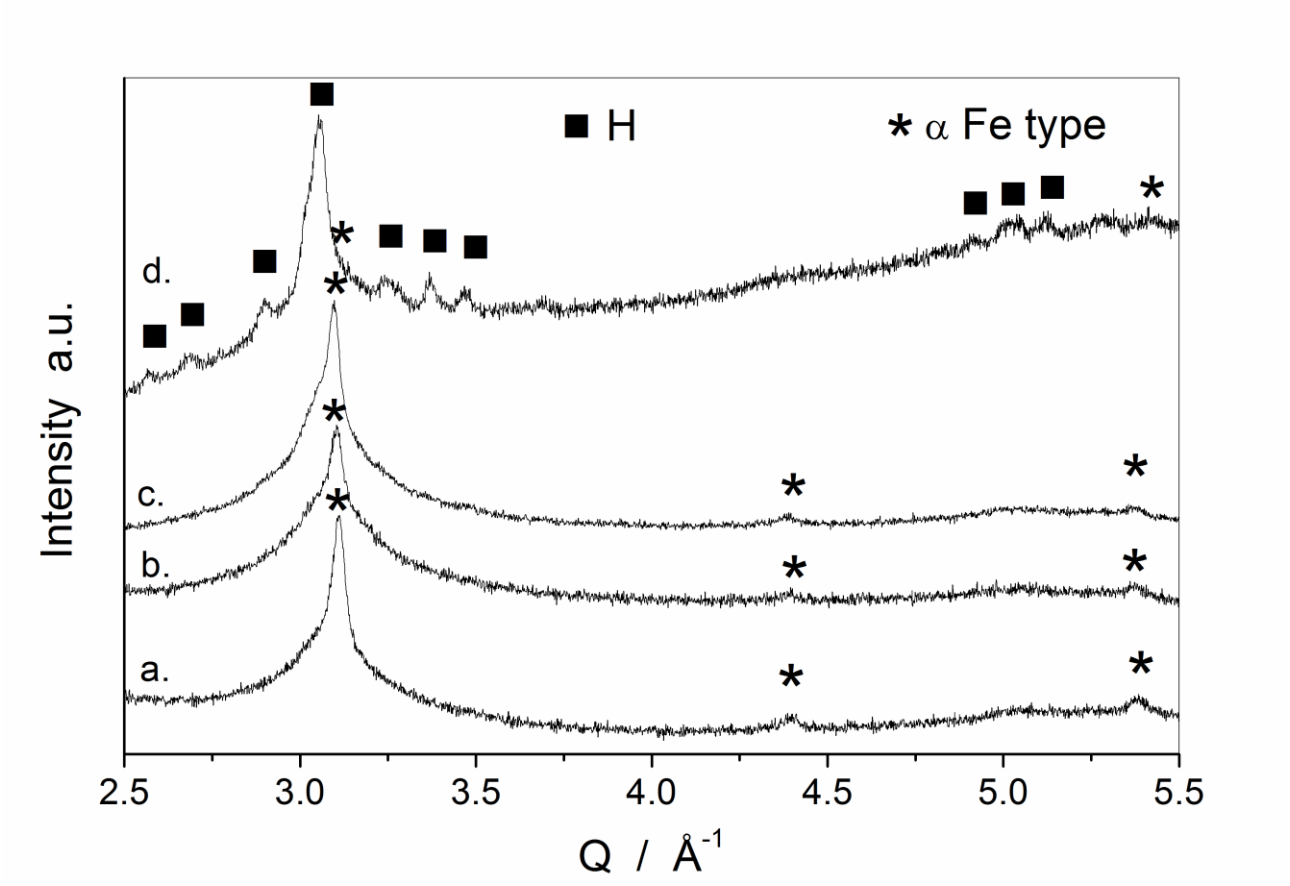

Fig. 4

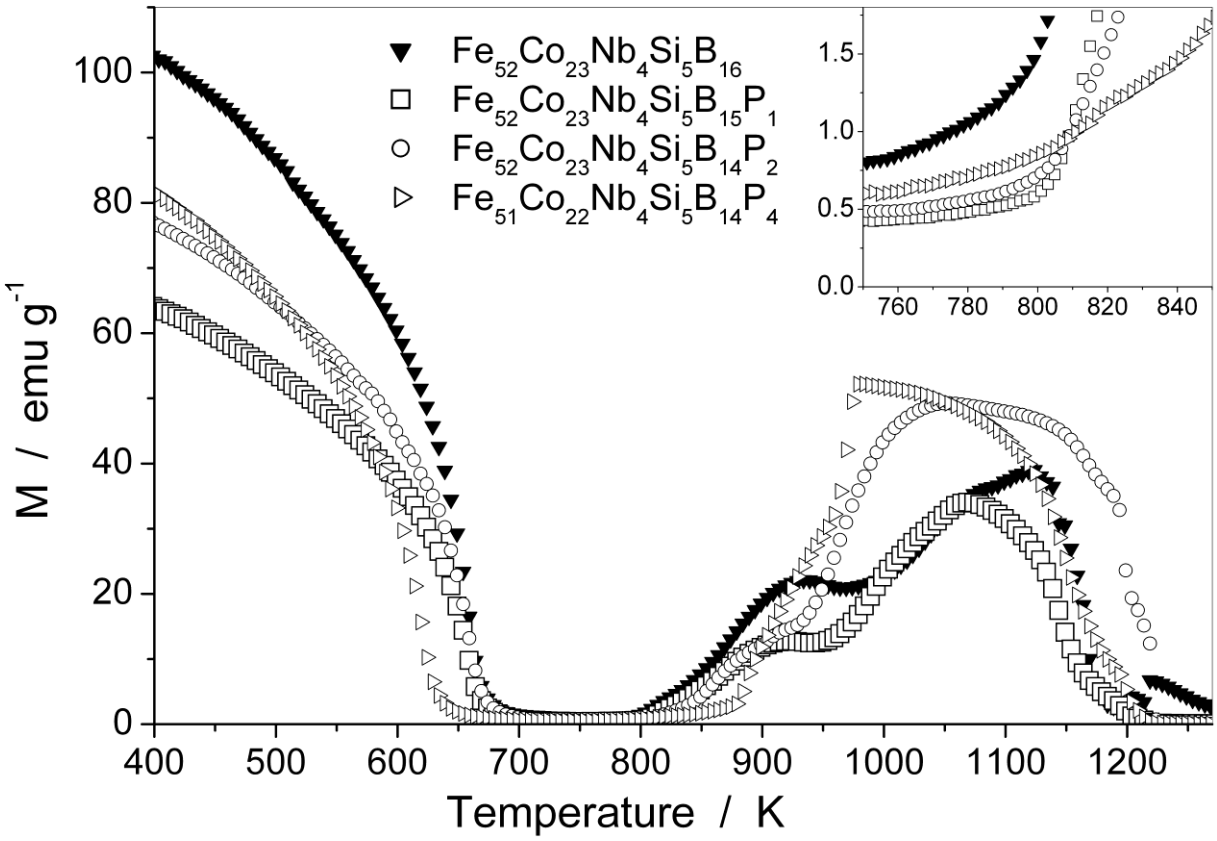
Fe52Co23Nb4Si5B16
Fe52Co23Nb4Si5B15P1
Fe52Co23Nb4Si5B14P2
Fe51Co22Nb4Si5B14P4
M / emu g-1
Temperature / K
0
20
40
60
80
100
400
500
600
700
800
900
1000
1100
1200
0.0
0.5
1.0
1.5
760
780
800
820
840

Fig. 5

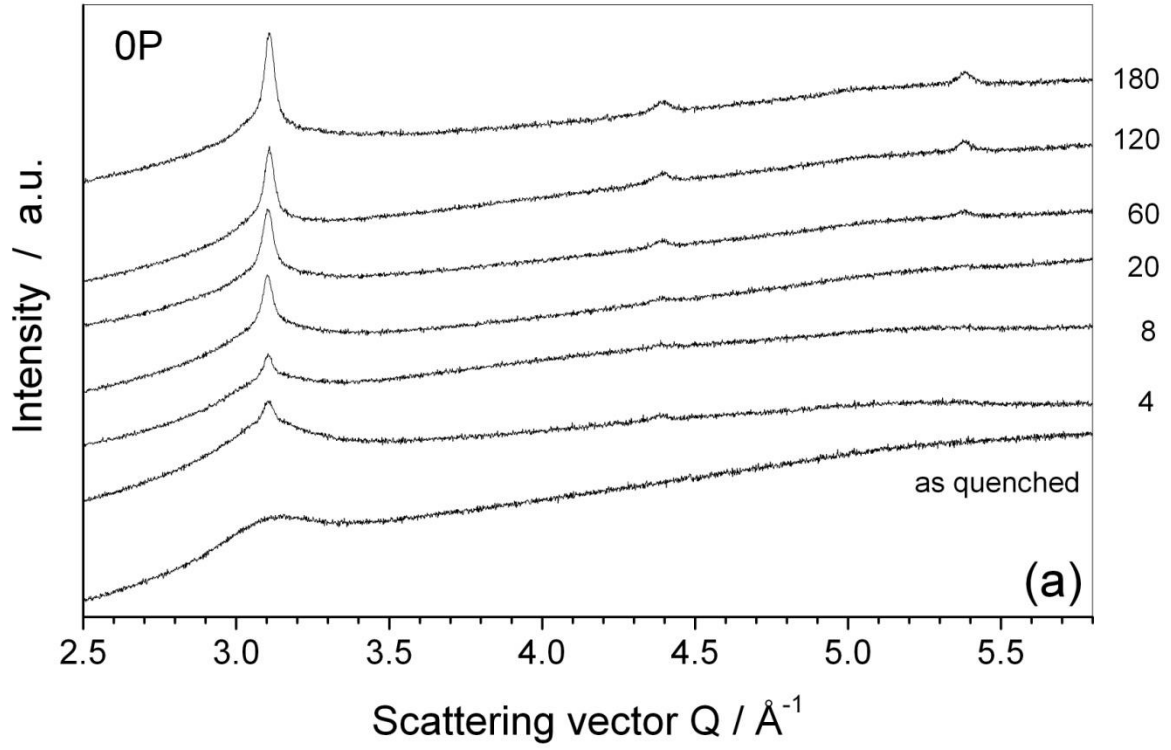
0P
180
120
60
20
8
4
as quenched
(a)
Intensity / a.u.
2.5
3.0
3.5
4.0
4.5
5.0
5.5
Scattering vector Q / Å-1

Fig. 6 a

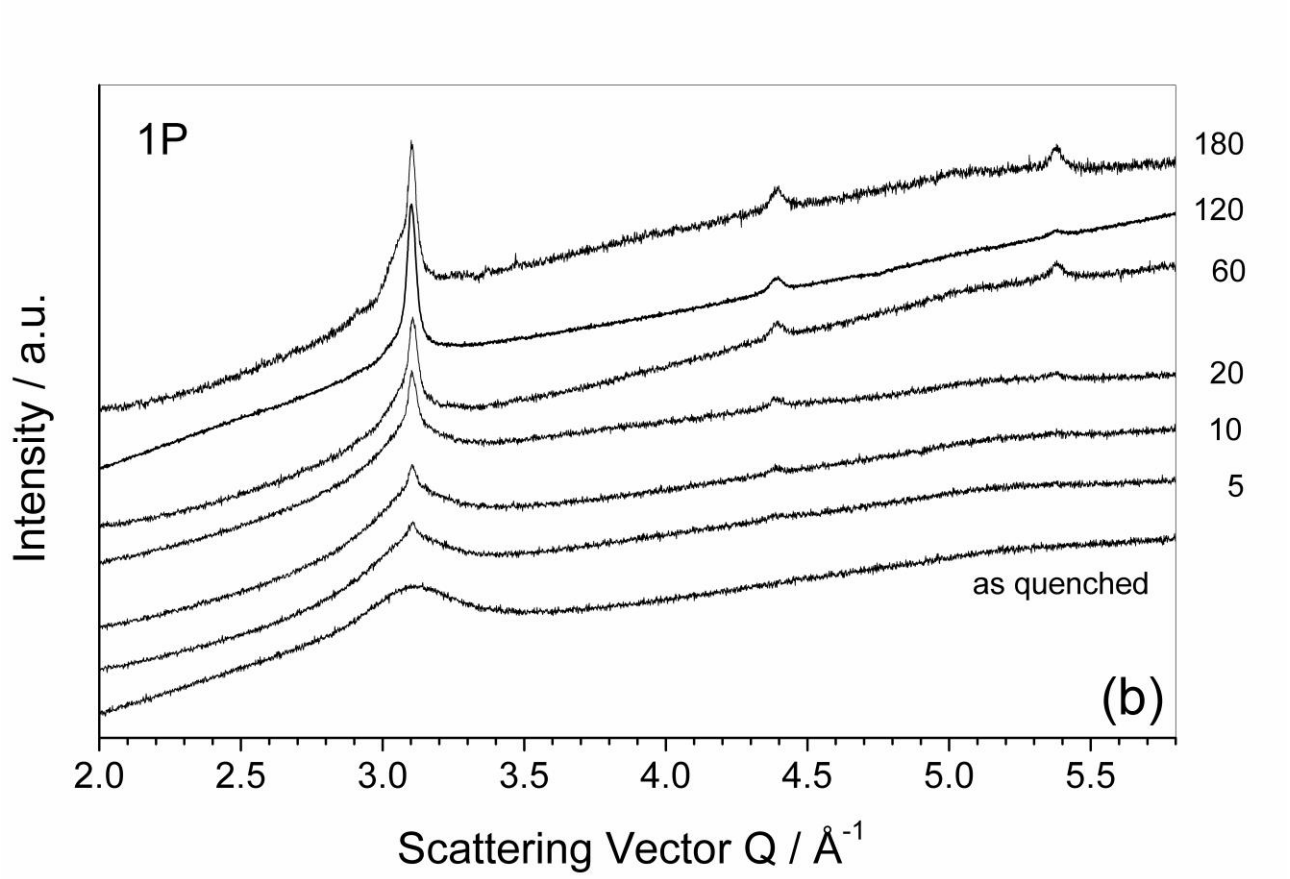
1P
180
120
60
20
10
5
as quenched
(b)
Intensity / a.u.
2.0
2.5
3.0
3.5
4.0
4.5
5.0
5.5
Scattering Vector Q / Å-1

Fig. 6 b

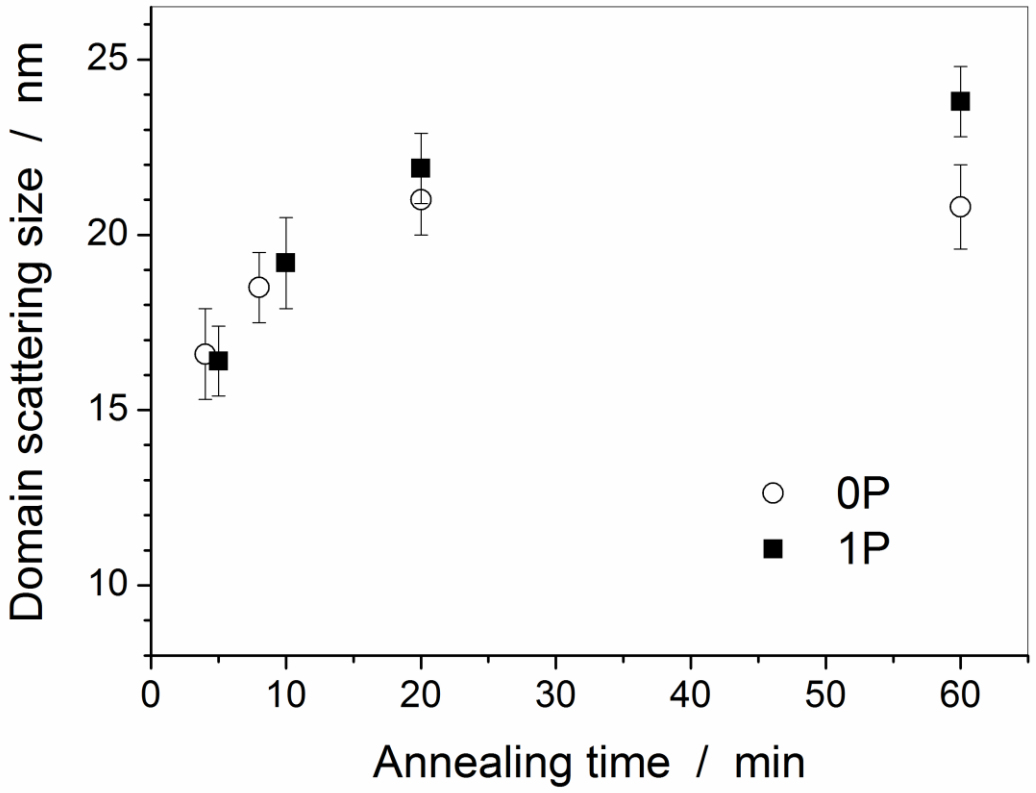
Domain scattering size / nm
25
20
15
10
0
10
20
30
40
50
60
Annealing time / min
0P
1P

Fig. 7

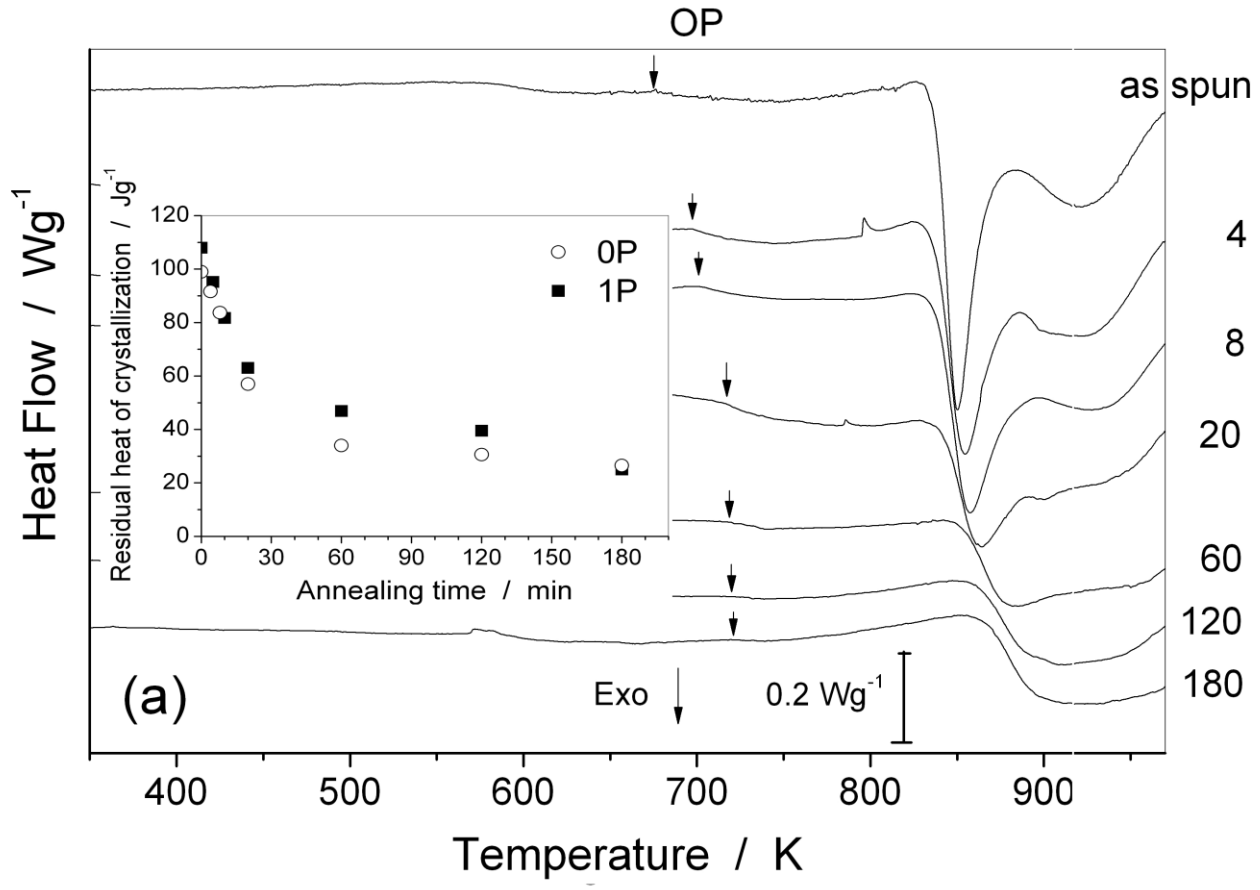
OP
as spun
4
8
20
60
120
180
Heat Flow / Wg-1
Residual heat of crystallization / Jg-1
0P
1P
Annealing time / min
(a)
Exo
0.2 Wg-1
Temperature / K

Fig. 8 a

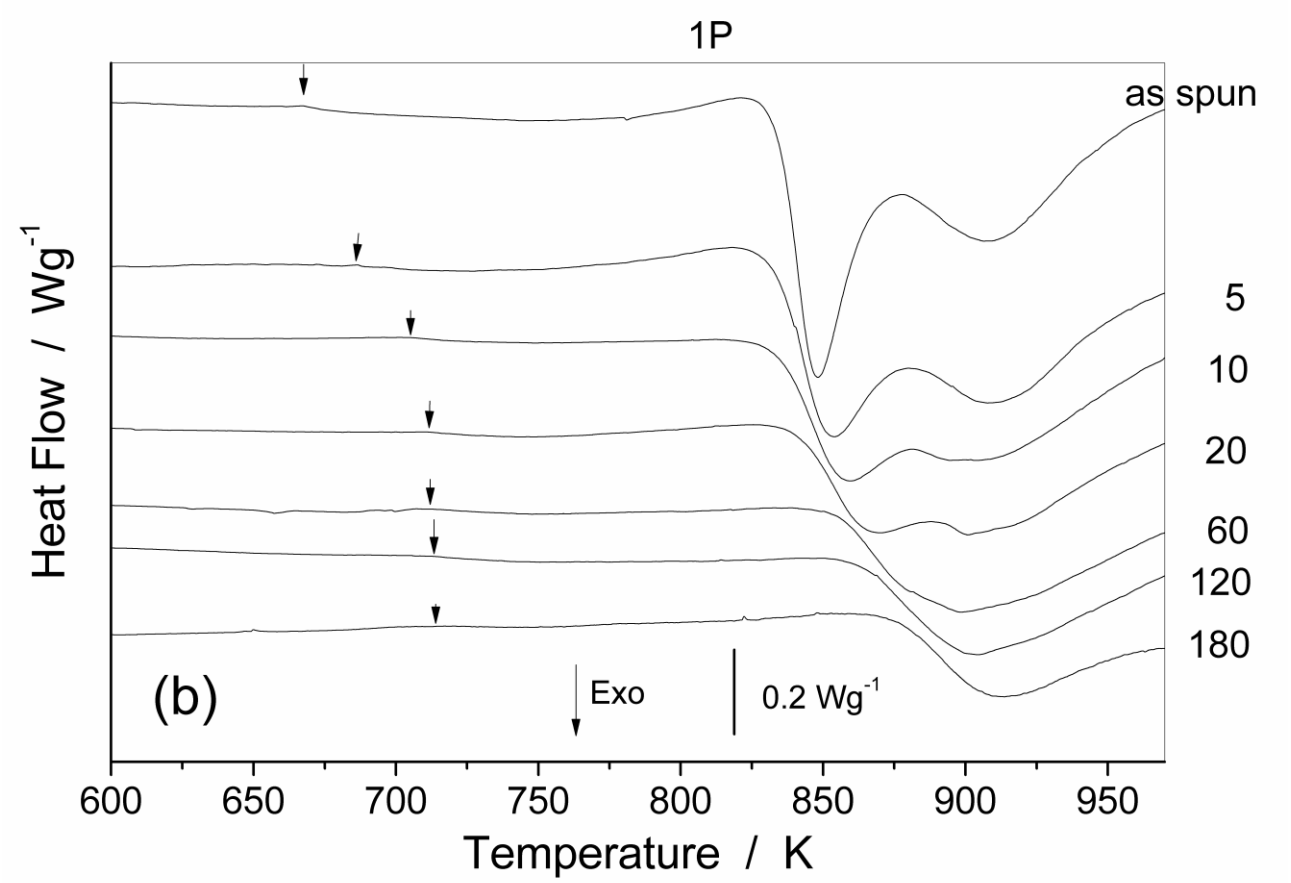
1P
as spun
5
10
20
60
120
180
(b)
Exo
0.2 Wg-1
Heat Flow / Wg-1
Temperature / K
600
650
700
750
800
850
900
950

Fig. 8 b

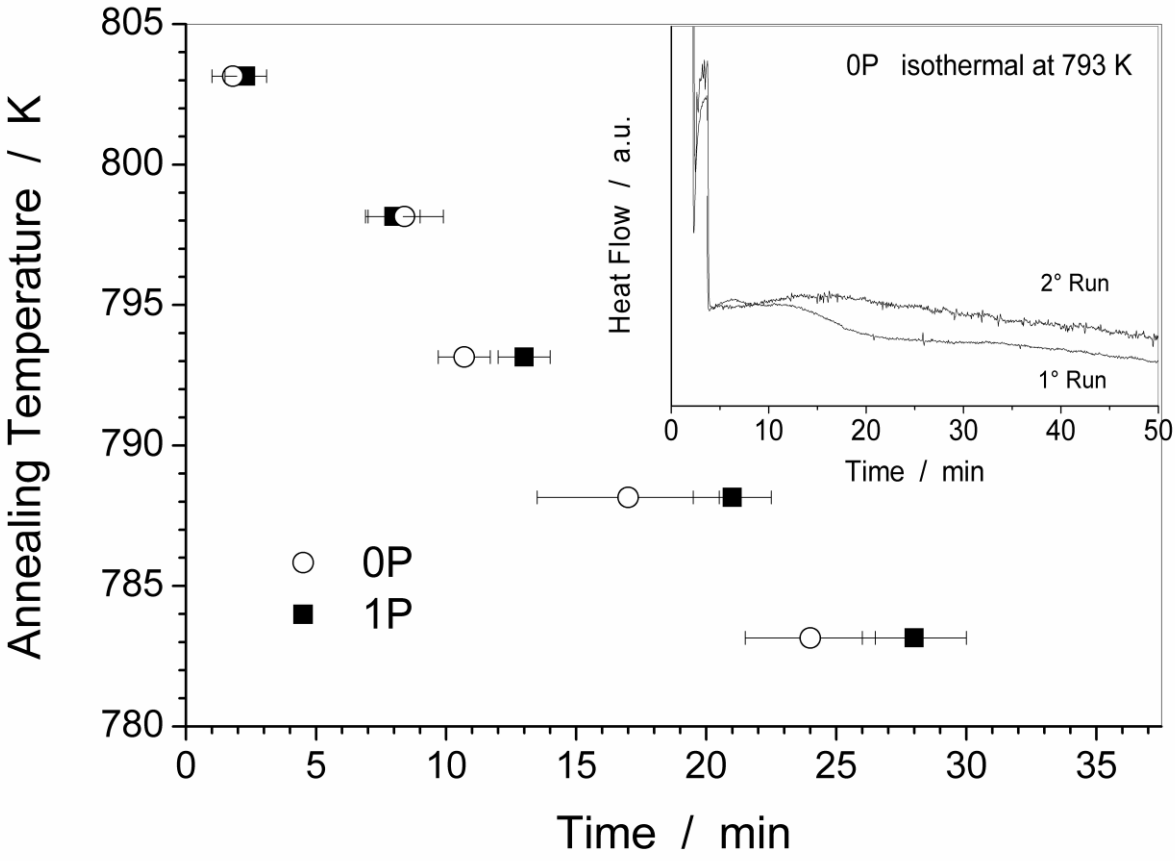
Annealing Temperature / K
805
800
795
790
785
780
0
5
10
15
20
25
30
35
Time / min
0P
1P
Heat Flow / a.u.
0P isothermal at 793 K
2° Run
1° Run
0
10
20
30
40
50
Time / min

Fig. 9

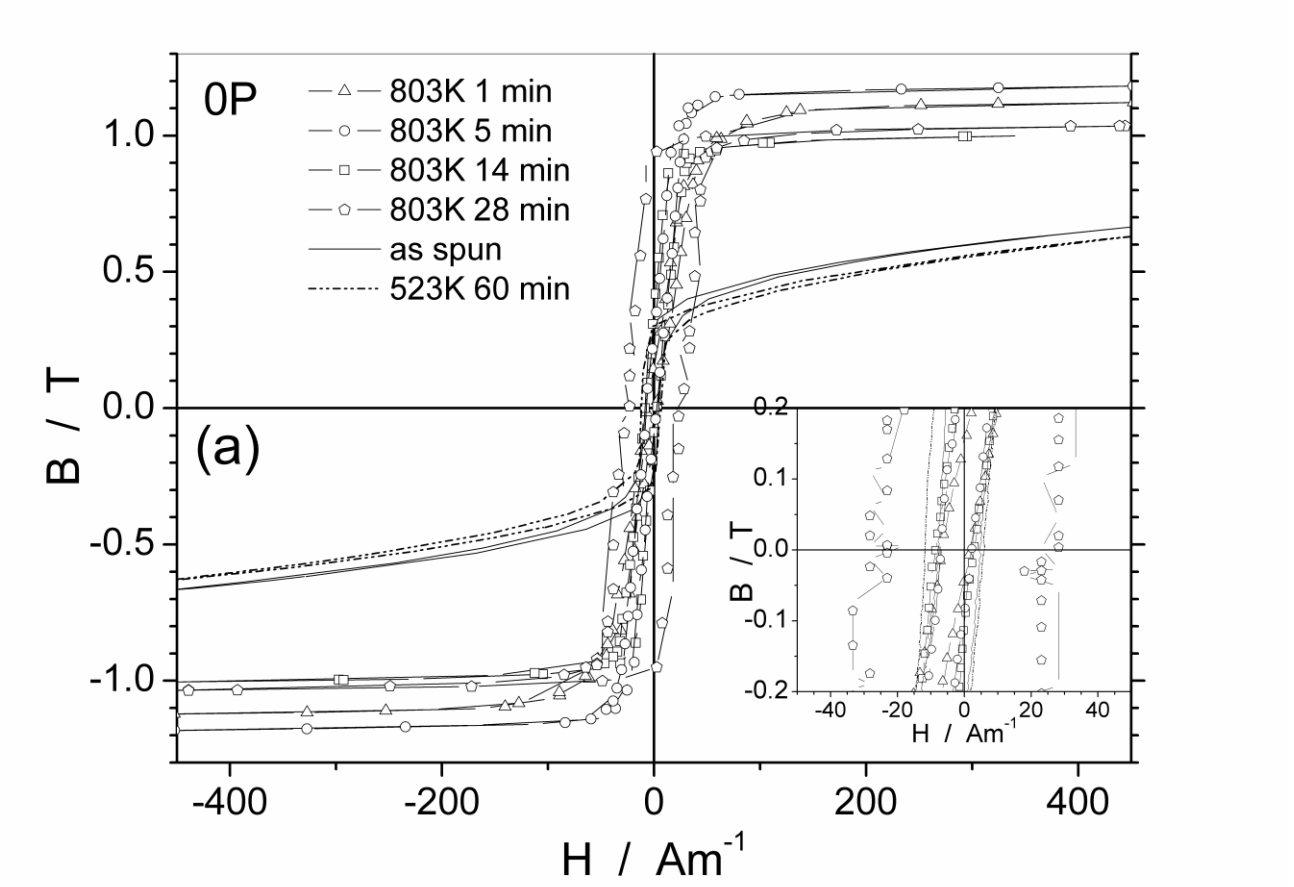
0P
803K 1 min
803K 5 min
803K 14 min
803K 28 min
as spun
523K 60 min
(a)
B / T
H / Am-1
1.0
0.5
0.0
-0.5
-1.0
-400
-200
0
200
400
0.2
0.1
0.0
-0.1
-0.2
-40
-20
0
20
40

Fig. 10 a

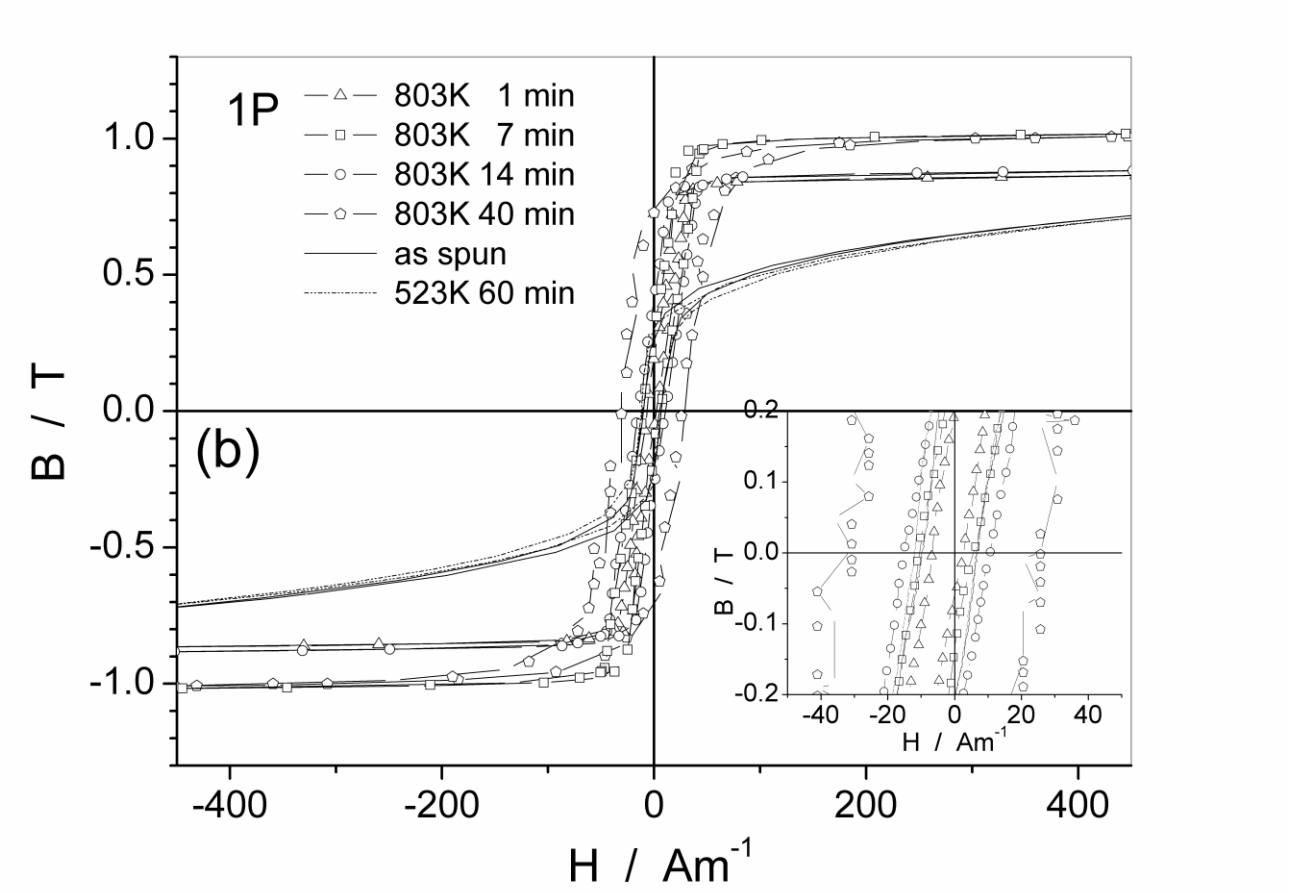
1P
803K 1 min
803K 7 min
803K 14 min
803K 40 min
as spun
523K 60 min
(b)
B / T
H / Am-1
1.0
0.5
0.0
-0.5
-1.0
-400
-200
0
200
400
0.2
0.1
0.0
-0.1
-0.2
-40
-20
0
20
40

Fig. 10 b

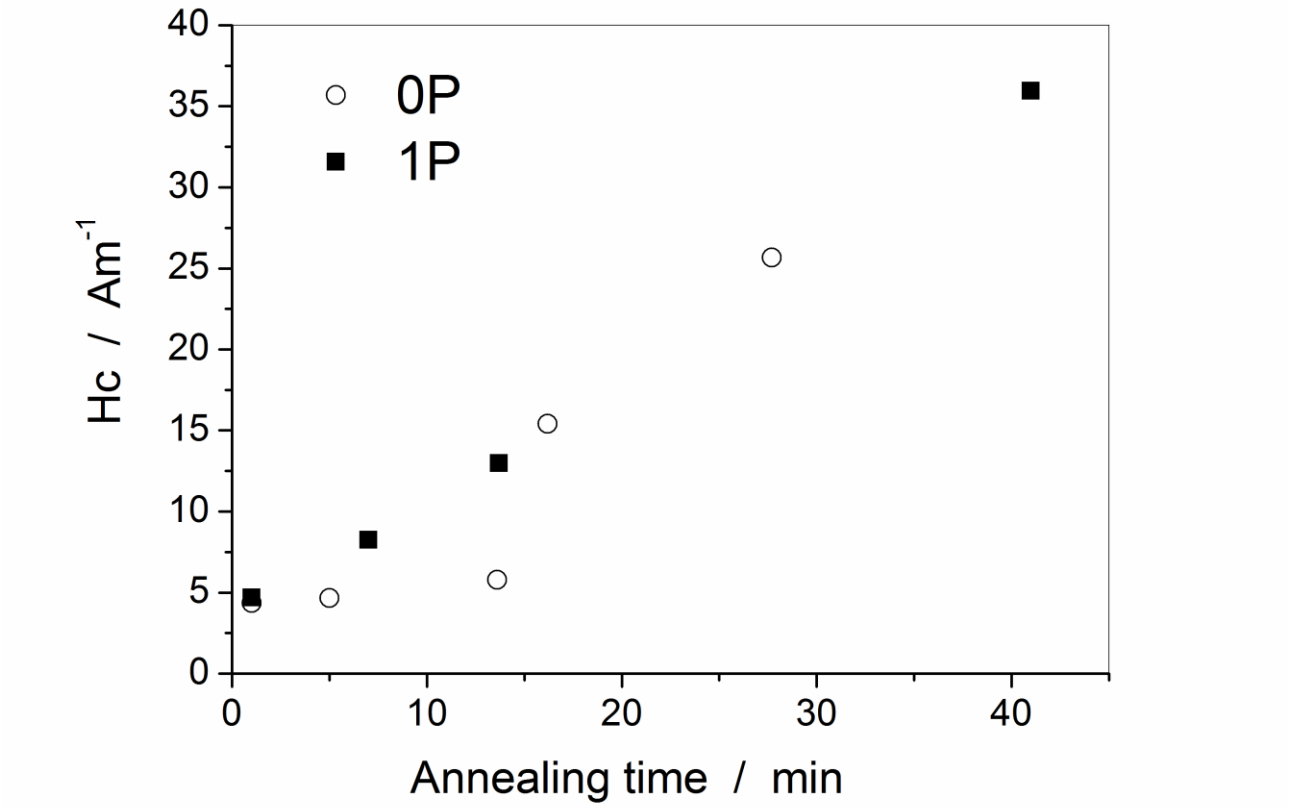
0P
1P
Hc / Am-1
Annealing time / min
0
5
10
15
20
25
30
35
40
0
10
20
30
40

Fig. 11

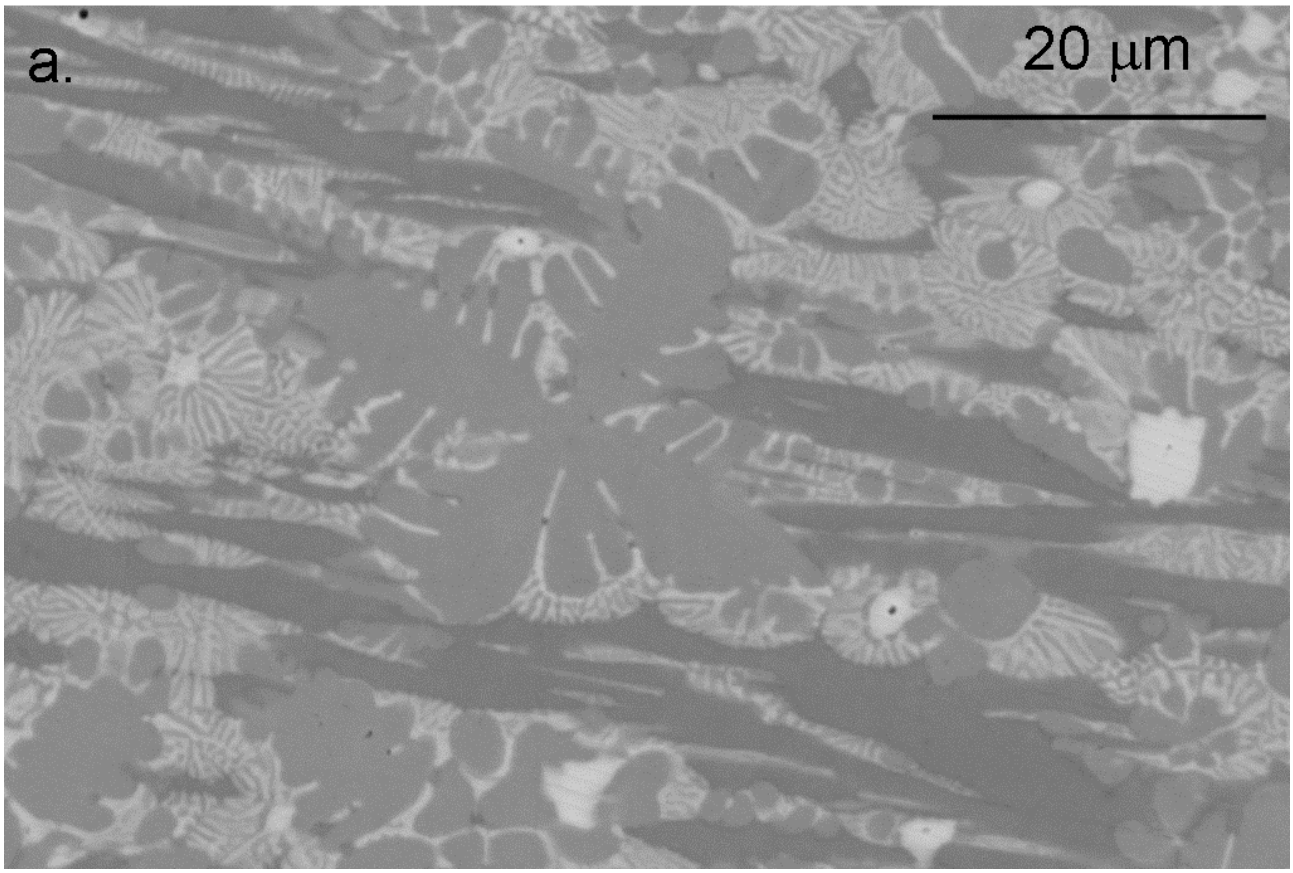

Fig. A a

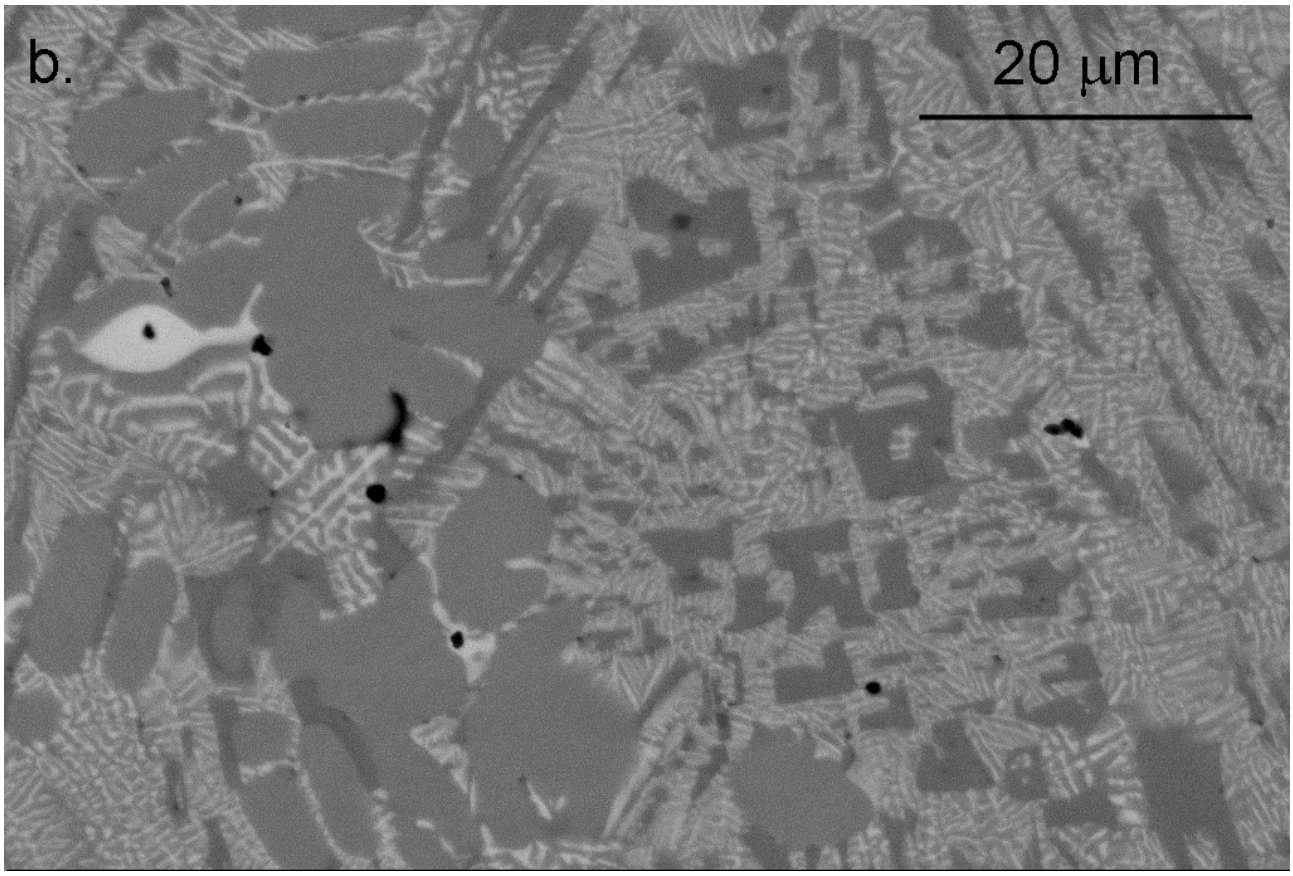

Fig. A b

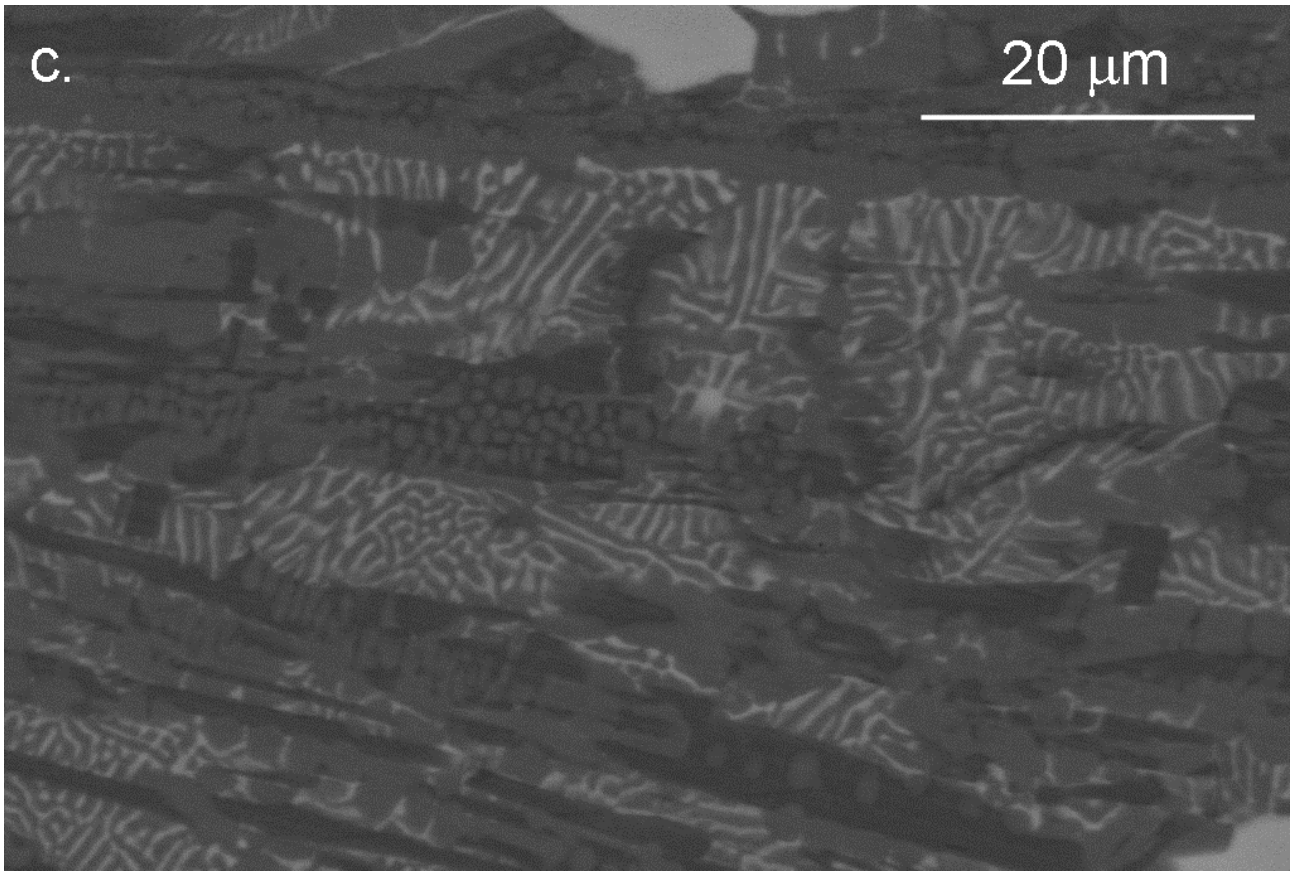

Fig. A c

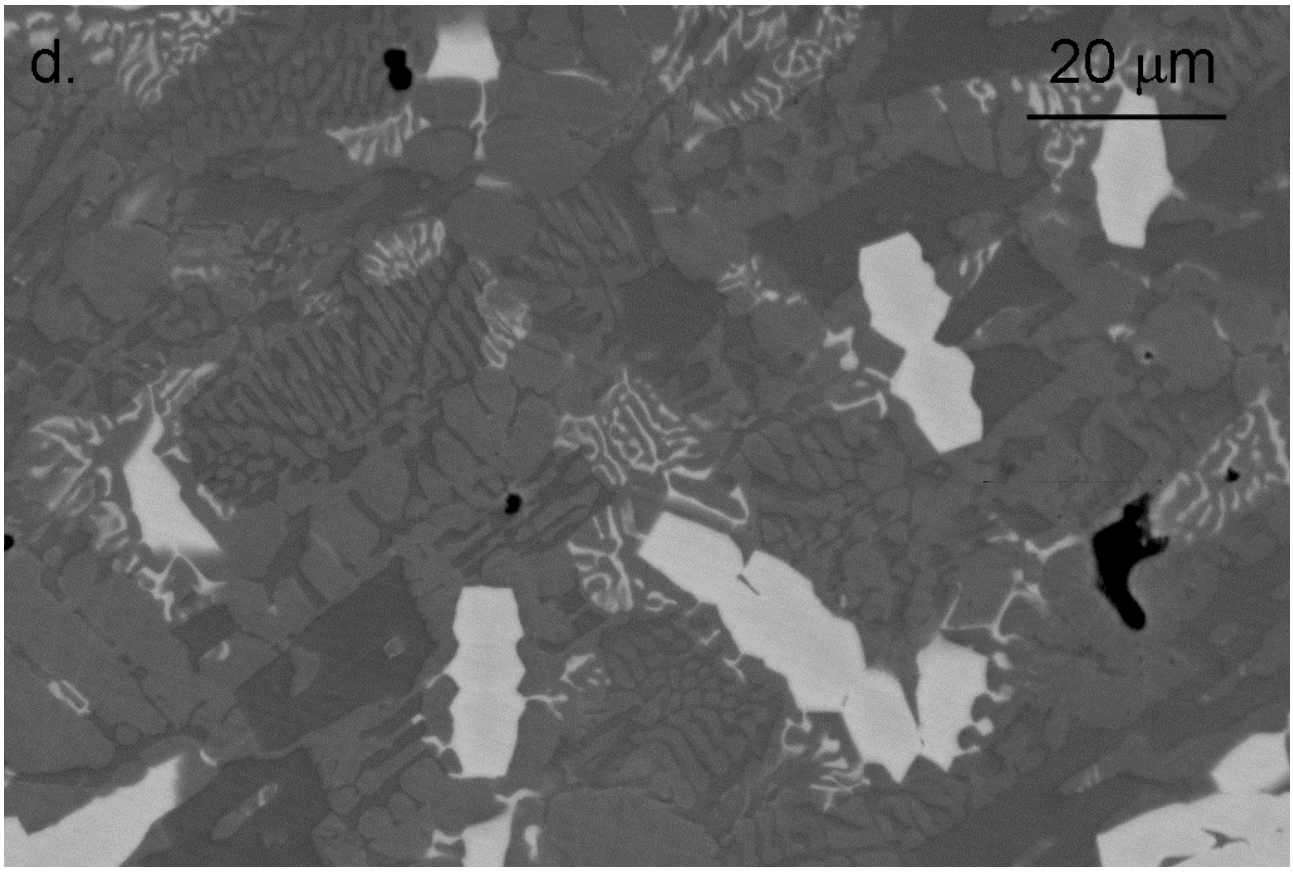

Fig. A d

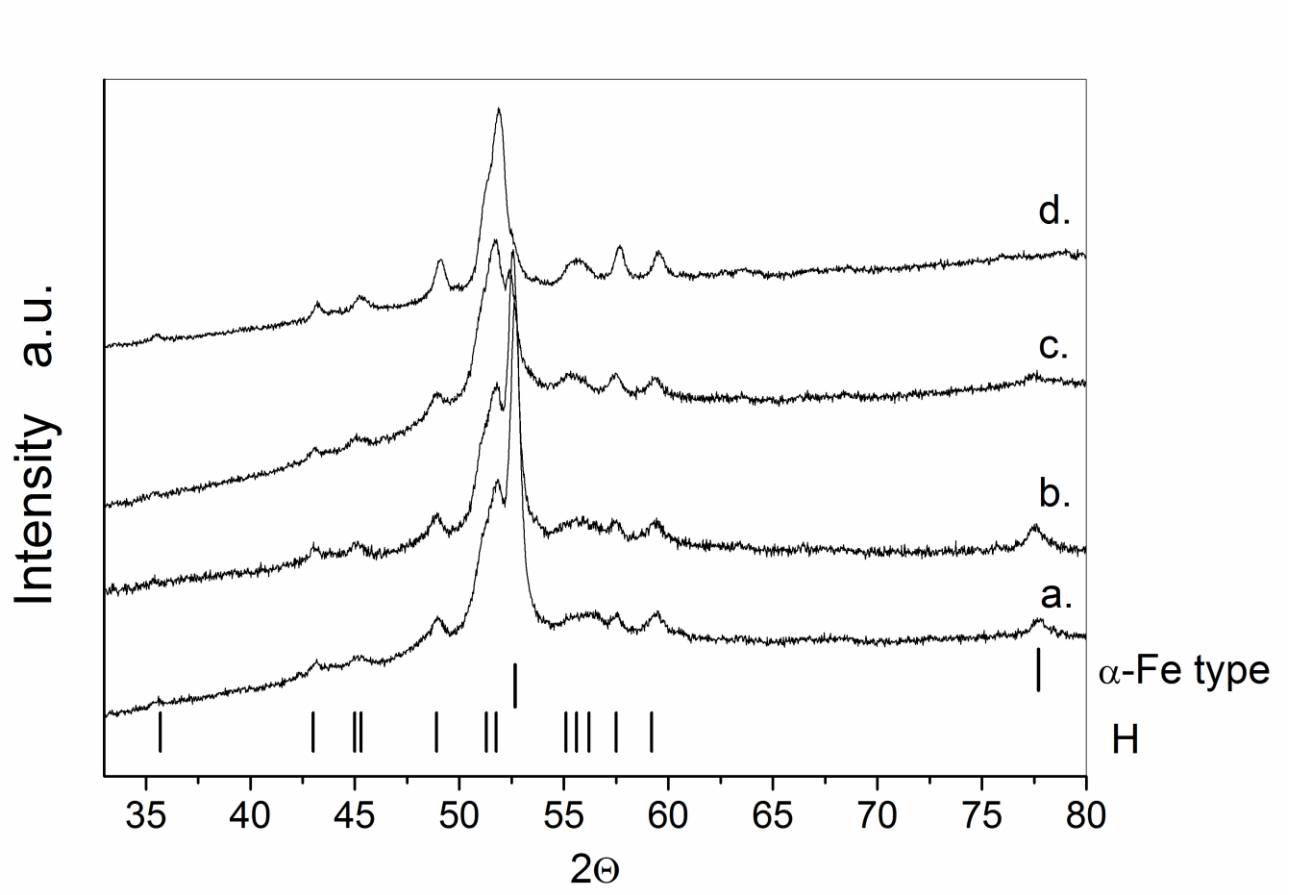

Fig. B

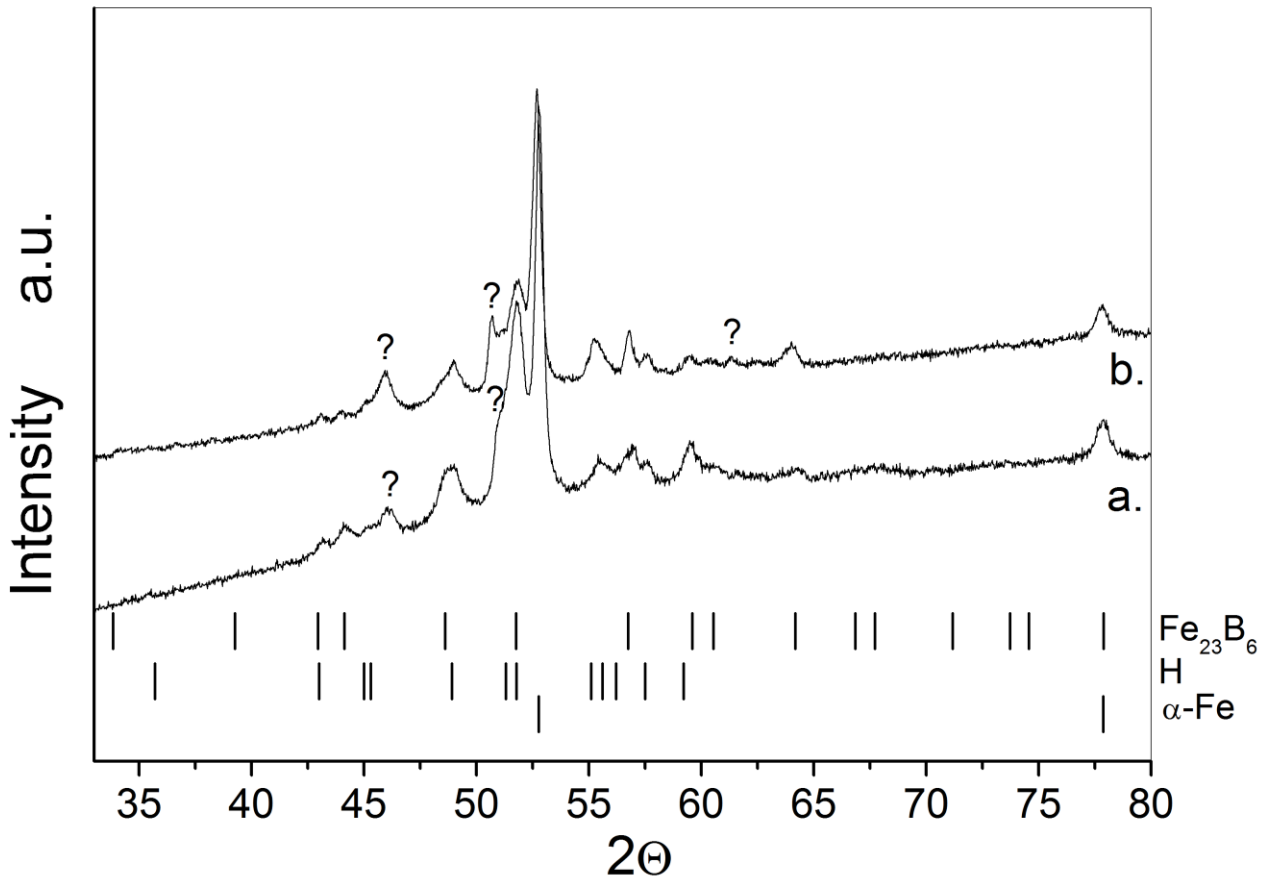

Fig. C